Supporting Information

A new catalyst based on the disposed red mud for the efficient electrochemical reduction of nitrate-to-ammonia

Yan-Tong Xu,[a] Ke-Cheng Ren,[a,b] Zui-Miao Tao,[a,b] Daniel Kobina Sam,[a,c] Enlang Feng,[d] Xiang Wang,[d] Gengming Zhang,[e] Junchi Wu [e] and Yan Cao*[a,b]

[a] Guangdong Provincial Key Laboratory of New and Renewable Energy Research and Development, Guangzhou Institute of Energy Conversion, Chinese Academy of Sciences, Guangzhou 510640, China. E-mail: caoyan@ms.giec.ac.cn
[b] College of Chemistry and Chemical Engineering, Anhui University, Hefei 230601, China.
[c] University of Science and Technology of China, Hefei 230026, China.
[d] Guangxi Huayin Aluminium Co., Ltd. Baise 533700, China.
[e] Geely Baikuang Group Research, Baise 533700, China.

Experimental Procedures

Material and chemicals

KNO_3 [≥ 99%, Aladdin], ethanol [99.8%, Aladdin], KH_2PO_4 [99.5%, Aladdin], K_2HPO_4 [99%, Aladdin], KOH [85%, Aladdin], NH_4Cl [99.999%, Aladdin], KNO_2 [97%, Aladdin], carbon cloth (CC) [W1S1009, CE-Tech Co., Ltd.], Ar gas [99.999%]. All chemicals were used as received without any purification.

Characterization

X-ray diffraction (XRD) was recorded with PANalytical X'Pert Pro MPD. X-ray photoelectron spectrums (XPS) were performed on ESCALAB 250Xi. Scanning electron microscopy (SEM) images were taken with a Hitachi S-4800 scanning electron microscope. Transmission electron microscopy (TEM) and corresponding energy-dispersive X-ray spectroscopy (EDS) images were obtained by the JEM-2100F transmission electron microscope with energy spectrometer. The concentration of NH_3/NH_4^+ analysis was detected on the ammonia nitrogen analyzer (AMTAX compact II type, HACH co.). The proton nuclear magnetic resonance (^1H-NMR) was measured on Bruker AVANCE III 400 MHz system. The analysis of metal element content of red mud was detected on inductively coupled plasma optical emission spectrometer (ICP-OES, OPTIMA 8000DV), in which the samples were fully dissolved by mixed acid solution (V(HF): V(HNO$_3$): V(HCl) = 4:1:3). 77 K N_2 sorption isotherms were recorded on Quantachrome Autosorb-iQ-2 apparatu.

Preparation of the working electrode

Massive red muds were ground in an agate mortar and sieved through a 125-μm mesh. The obtained red mud powders were washed by pure water 24 h using a Soxhlet extractor to remove the water-soluble impurities. And then the red muds were dried in an oven at 60 °C.

5 mg red muds were dispersed in 1.2 mL of 1:1 v/v water/ethanol with 20 μL Nafion by one-hour sonication to form a homogeneous suspension. CC (1×1 cm^2) was clean by anhydrous alcohol and deionized water for 1 h through ultrasonication prior to red mud deposition. Then the red mud ink was dropped onto carbon cloth to yield a red mud loading of 0.8 mg cm^{-2}. As for the pure Fe_2O_3, the mass loading was reduced to 0.24 mg cm-2 to ensure the same Fe content on working electrode with RM one.

Electrochemical measurements

All electrochemical tests were performed on ZAHNER PP211 and CHI760 electrochemical workstations. The electrolyte solution was bubbled by Ar flow for at least 30 min prior to electrochemical experiments. The electrocatalysis test were performed in a gas-tight H-cells separated by proton exchange membrane (Nafion 211) at room temperature.

The proton exchange membranes were activated in dilute 5 wt% H_2SO_4 aqueous solution at 80 °C for 0.5 h, and then washed by copious amounts of water and soaked in distilled water for at least 3 h. 15 mL of electrolyte was used in the cathodic chamber.

For the three-electrode system, an ultra-pure graphite rod and an Ag/AgCl electrode saturated KCl solution (E(Ag/AgCl) = 0.197 V) were employed as the counter electrode and the reference electrode, respectively. A red mud coated CC (1×1 cm^2) was the working electrode. All potentials in this work were expressed in the reference of RHE, which can be calculated by the Nernst equation:

$$E(\text{RHE}) = E(\text{experiment}) + 0.059\text{pH} + E(\text{Ag/AgCl})$$

where E(RHE) is the converted potential and E(experiment) is the measured potential.

For the three-electrode system, a nickel foam was used as anode and 1 M KOH aqueous solution as anodic electrolyte.

All linear sweep voltammetry (LSV) curves were tested with a scan rate of 10 mV s^{-1} without iR compensation. The catalytic performance was evaluate under chronoamperometry mode for 0.5 h with magnetic stirring (900rpm).

Solar-driven NARR tests were powered by the ABET Sun 3000 solar simulator at different light intensities (0.04, 0.05, 0.06, 0.07, 0.08, 0.09 and 0.10 W cm^{-2}) for 30 mins.

The FE_{NH3}, r_{NH3}, EE_{NH3}, $EE_{Solar-to-NH3}$ were calculated according to the following equations:

$$FE_{NH3} (\%) = 8 \times F \times c(NH_3) \times V / Q \times 100\%$$

$$r_{NH3} (\text{mmol cm}^{-2} \text{ h}^{-1}) = c(NH3) \times V / (A \times t)$$

$$EE_{NH3} (\%) = c(NH_3) \times V \times \Delta_r H_m / (U \times I \times t)$$

$$EE_{Solar-to-NH3} (\%) = c(NH_3) \times V \times \Delta_r H_m / (L \times A_{PVC})$$

where F is the Faradaic efficiency, 96485 C mol^{-1}; $c(NH_3)$ is the concentration of NH$_3$; V is the volume of cathodic electrolyte, 15 mL; Q is the integrated charge during NARR test; A is the electrode surface area, 1 cm^2; t is the electrolysis time, 1800 s; $\Delta_r H_m$ is calculated according to the overall reaction of $KNO_3 + 2H_2O \rightarrow NH_3(g) + KOH + 2O_2(g)$, 595.5 kJ mol^{-1}; U is the total cell voltage; I is the electrolysis current; L is the light intensity of sun simulator; A_{PVC} is the area of the photovoltaic cell, 210 cm^2.

For the long-term recycle test, electrolysis under −0.73 V (vs. RHE) lasting 4 hours for each cycle was performed by chronoamperometry with the electrolyte containing 1.0 M PBS and 1.0 M KNO$_3$. After finishing electrolysis of each cycle, we replaced the electrolyte with a refresh one while the same working electrode is maintained for the next cycle.


Ammonia detection and quantification

1 mL sample solution was diluted into 10 mL prior to NH_3 detecting. The concentration of NH_3 was determined according to colorimetric methods by an ammonia nitrogen analyzer (HACH AMTAX compact II type). The calibration curve between concentration of NH_3/NH_4^+ and absorbance was shown as follow:
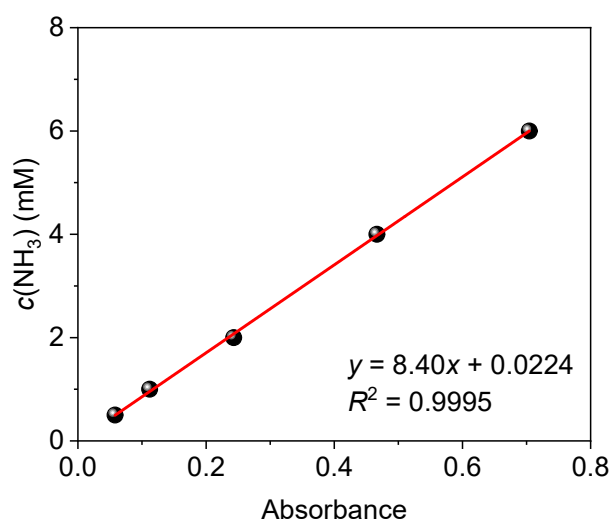
Nitrite detection and quantification.

1 mL sample solution was diluted into 10 mL prior to NO_2^- detecting. 0.4 mL sulfanilic acid solution (4 g/L sulfanilic acid in 20% HCl) was mixed with 10 mL nitrite-containing sample. After standing for 5 mins, 0.2 mL *N*-(1-naphthyl)-ethylenediamine dihydrochloride solution (2 g/L) was added and the mixture was further stand for 15 mins. Finally, the solution was detected at 550 nm. The calibration curve between concentration of NO_2^- and absorbance was shown as follow:
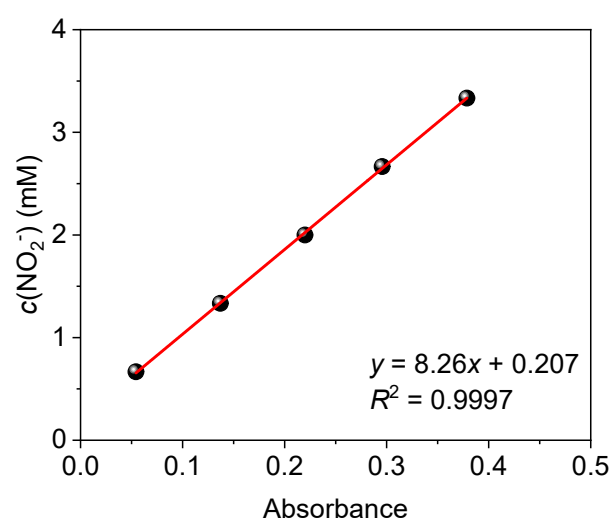
Explanation on the FE_{NH3} evolutions upon nitrate concentrations and electrolysis times

The insight of FE_{NH3} evolutions upon nitrate concentrations and electrolysis time are probably related to the evolution of reactants and products in the electrolyte solution. Notably, the electrolysis cell is a closed system, leading

all concentrations of reactants, products and by-products changes along the electrolysis time. And the reaction pathway of NARR on the catalyst surface could likely be a stepwise hydrogenation process: $*NO_3 + *H_2O \rightarrow *NO_xH_y \rightarrow *NH_3$. Meanwhile, there is a competing side reaction potentially: $*H_2O \rightarrow *H_2$. And the surface coverage (ϑ) of $*NO_3$ (ϑ_{NO3}), $*H_2O$ (ϑ_{H2O}) and $*NH_3$ (ϑ_{NH3}) are respectively related to concentrations of reactants and products based on their adsorption equilibriums thermodynamically.

Initially only $*NO_3$ and $*H_2O$ exist on the catalyst surface, in favor for its transformation toward the intermediate $*NO_xH_y$. And the formation of $*NH_3$ is naturally accelerated upon the increase of ϑ of $*NO_xH_y$ (ϑ_{NOxHy}). As the reaction proceeds and the NH_3 concentration increases, the forward of the reaction toward $*NH_3$ is gradually balanced by the backward one and responds a drop in FE_{NH3} consequently. Therefore, the highest FE_{NH3} is achieves at the first 30 mins and declines along reaction time prolonging in Fig. S9. By the way, this is also the reason that FE_{NH3} per cycle in the long-term recycling test is lower than 92.8%.

Effect on concentration can be explained by a similar mechanism. The concentration of NO_3^- determines ϑ of $*NO_3$ (ϑ_{NO3}) on the catalyst surface, also involving $*H_2O$ (ϑ_{H2O}) in the electrolyte. The raising NO_3^- concentration increases ϑ_{NO3}, while naturally decreases ϑ_{H2O}. A relatively low ϑ_{NO3} likely inhibits NARR by some side reactions (such as HER). Conversely, a decreased ϑ_{H2O} (available activated hydrogen) further likely resulted in the incomplete hydrogenation of NO_3^-. Therefore, the increase of nitrate concentration results in the drop of FE_{NH3}. A 1.0 M in nitrate concentration here is just around the critical point and provides an optimal ratio of $\vartheta_{NO3}/\vartheta_{H2O}$, as thus a highest FE_{NH3}.

The motivation of the initial water washing operation for RM sample

The RM contains a number of contaminants. We removed water soluble part, such as residual alkali, mainly because of the NARR tests in aqueous solution, where the water-soluble contaminations might be dissolved by the electrolyte solution to impact NARR tests regarding likely effects on the surface structures of RM samples and the NARR pathway and performance. With these concerns, we performed the water-washing procedure to remove the water-soluble contaminants on the RM surface prior to be as NARR catalysts.

Involvement of different components in RM for NARR

Among different metal oxides species in RM, Fe_2O_3 severs as the major active species as NARR catalysis while Ti atoms intergrown in Fe_2O_3 lattices synergistically help to promote its NARR activity and the NH_3 selectivity. While, Al_xSi_yO species (such as AlOOH in RM, Cancrinite and Katoite) serve as porous matrixes to support catalysts, increasing active surface area.

The reason of suppressing the HER

(1) As we known, the acidic media can promote the HER process for most of HER catalysts, those catalysts can merely perform outstandingly in the neutral condition. Thus, the neutral pH environment in this study helps the suppression of its HER activity to some extent.

(2) As for the presence of nitrate, on the one hand, the competitive adsorption of $*NO_3$ reduces the similar $*H$ adsorption and its surface coverage, consequently decreasing the tendency from $*H$ toward H_2. Moreover, the proton transfer energy can be decreased by switching the reaction pathway from HER to NARR, resulting in selective reaction toward NARR (*J. Mater. Chem. A*, **2022**, DOI: 10.1039/D2TA04707A).
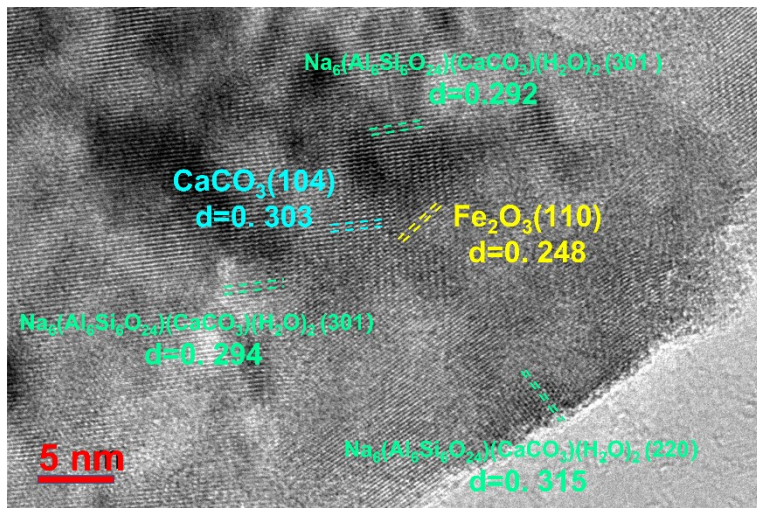
Fig. S1 HRTEM image of RM. For image filtering, the selected local regions were firstly performed a Fast Fourier Transform (FFT) followed by an inverse FFT using the Gatan Digital Micrographic. And then the lattice spacing was directly measured by the line profile tool and calculated by averaging the results over at least three periods.

Fig. S2 HRTEM image of RM.

724.53 eV

710.96 eV

Fe2p$_{1/2}$
Fe2p$_{3/2}$
Satellite
○ Experiment
— Fitting

Binding energy (eV)
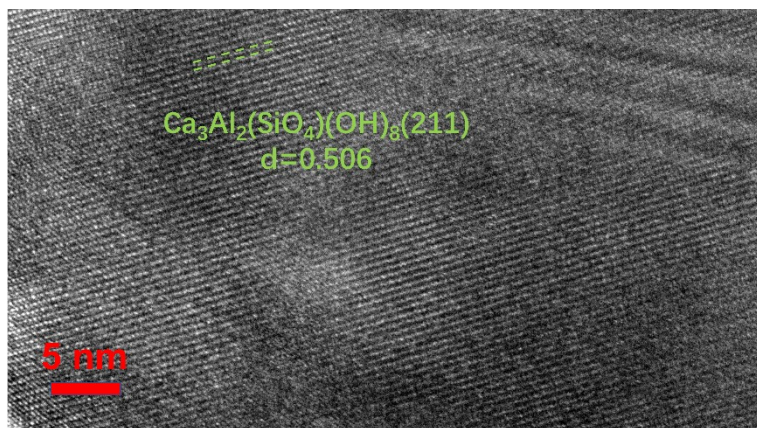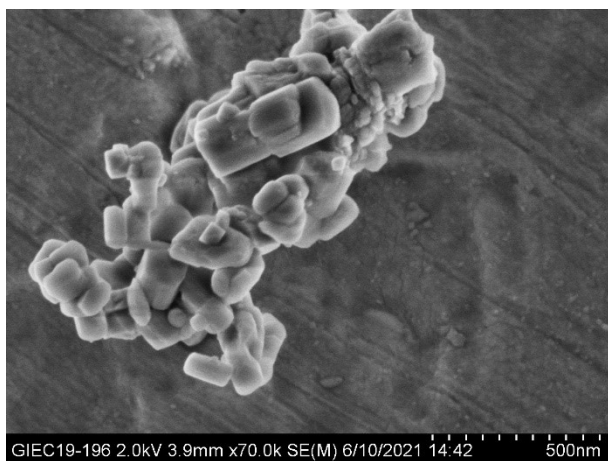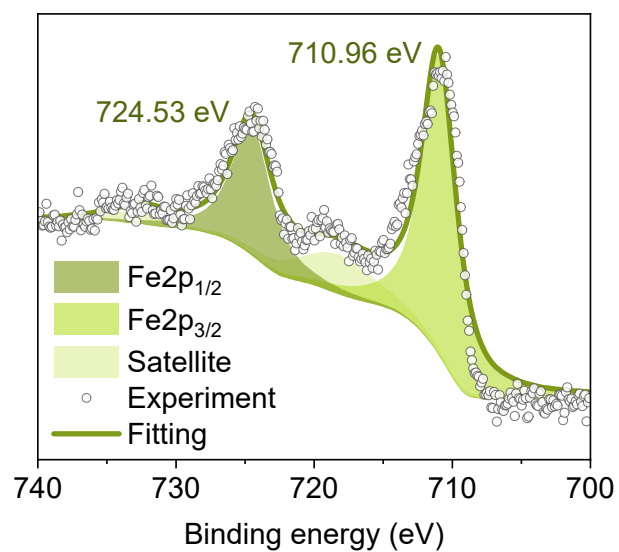
Fig. S4 High resolution Fe2p XPS profile for RM.

6.1%

6.2%

7.1%

Others

TiO$_2$

Na$_2$O

29.2%

Fe$_2$O$_3$

13%

CaO

SiO$_2$

Al$_2$O$_3$

20%

18.4%
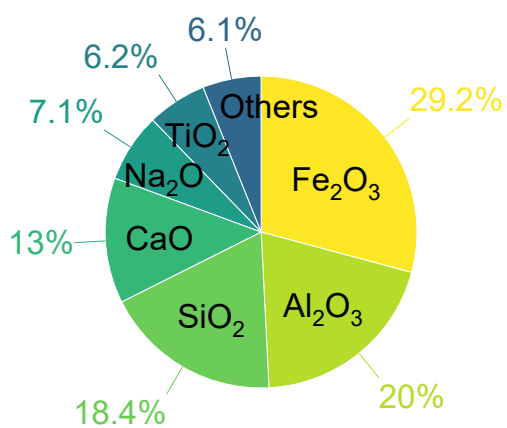
Fig. S5 Compositions of RM based on ICP-OES.
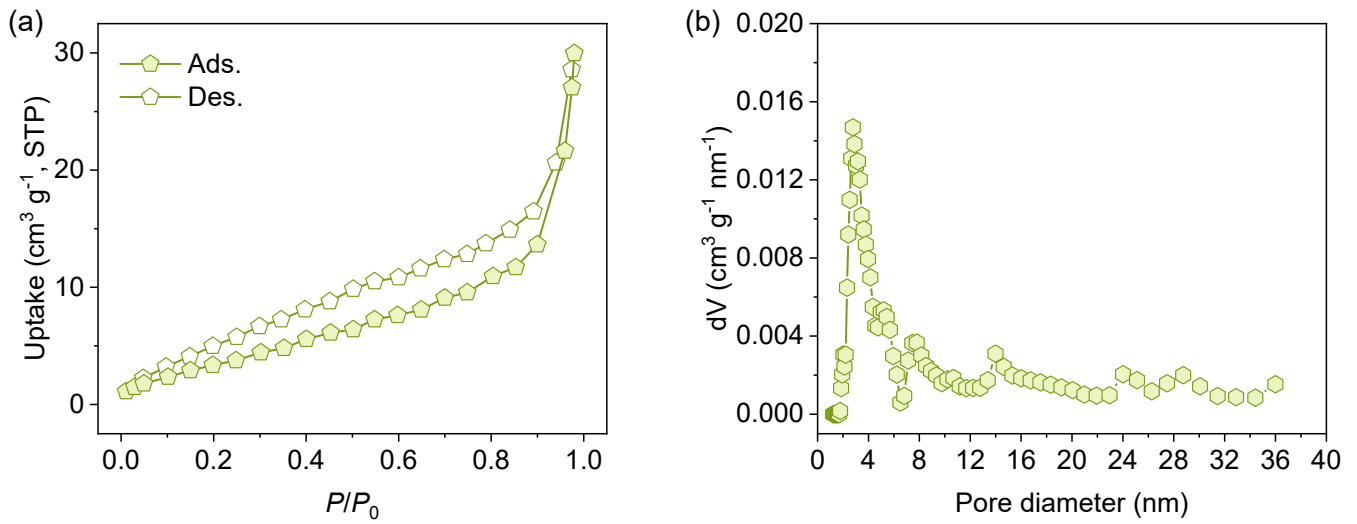
Fig. S6 (a) 77 K N_2 sorption isotherms of RM and (b) the corresponding pore diameter distribution.
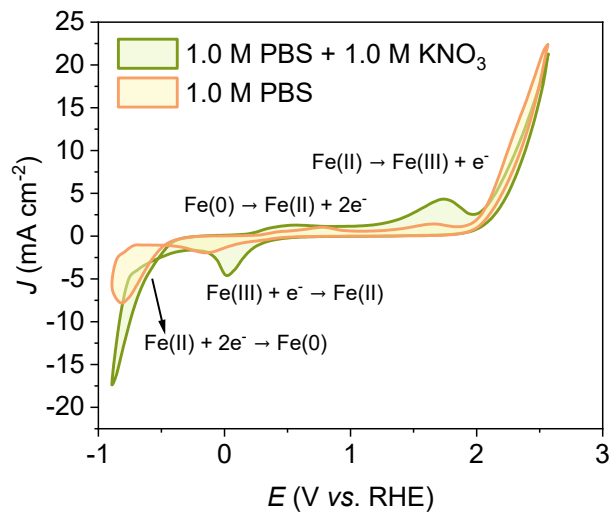
Fig. S7 CV curves for RM in 1 M PBS with and without KNO_3. Notably, a dramatic increase on current response is observed in the presence of nitrate. However, both oxidation and reduction peaks also can be observed in the absence of nitrate, demonstrating those peaks are not associated with nitrate. Associating with previous reports (*Sci. Rep.*, **2021**, *11*, 5185), it seemed to be related to an electrode surface process and not to charge transfer processes with nitrate. These peaks can be associated to ferric reduction and iron oxidation, as marked in the Figure.
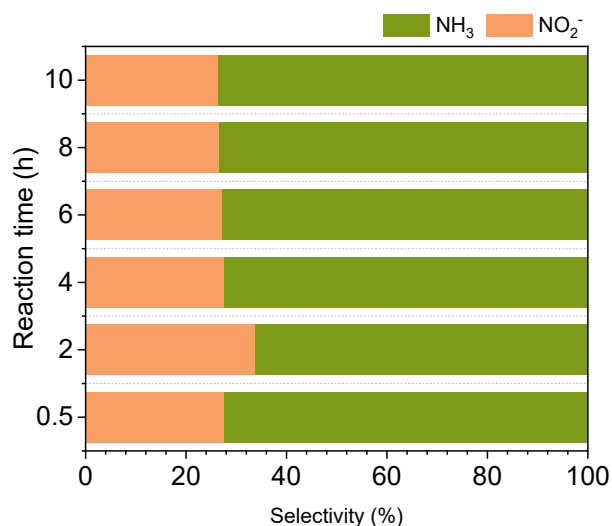
Fig. S8 Selectivities of NH_3 and NO_2^- during NARR. Notably, the current closed electrolysis system maintains the changing concentrations of all species in its reaction operation. Regarding the NO_2^- as the incomplete hydrogenation product in the NARR process, the chemical equilibrium on the electrode surface can be simplified as "$*NO_3 \rightleftharpoons *NO_2 \rightleftharpoons *NH_3$". The initial coverages of $*NO_2$ and $*NH_3$ are 0, and it exhibits the intrinsic catalytic activity and a higher NH_3 selectivity at the initial 30 mins, which is reasonably set as the reaction time for the evaluation of the catalyst activity. The further prolonged until 2 h starts the gradual $*NH_3$ accumulation likely increases the suppression of the $*NO_2$ to $*NH_3$ conversion, affording an increased selectivity toward NO_2^-. Similarly, the increased coverage of $*NO_2$ will accelerate the NH_3 production, leading a gradually increased NH_3 selectivity after 2 h. This mechanism consequently determines the drop and later recovered NH_3 selectivity.
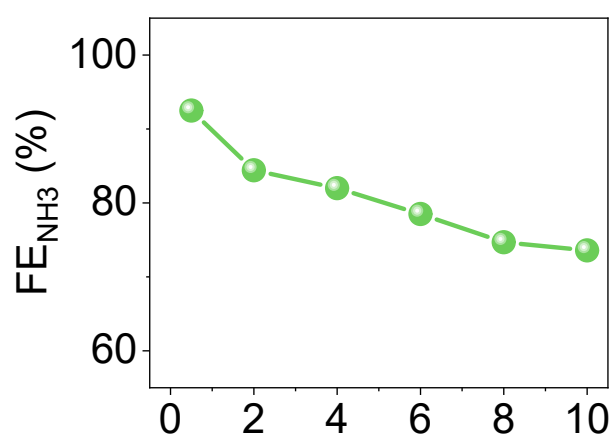

Fig. S9 FE_{NH3} evolution along the electrolysis time prolonging.
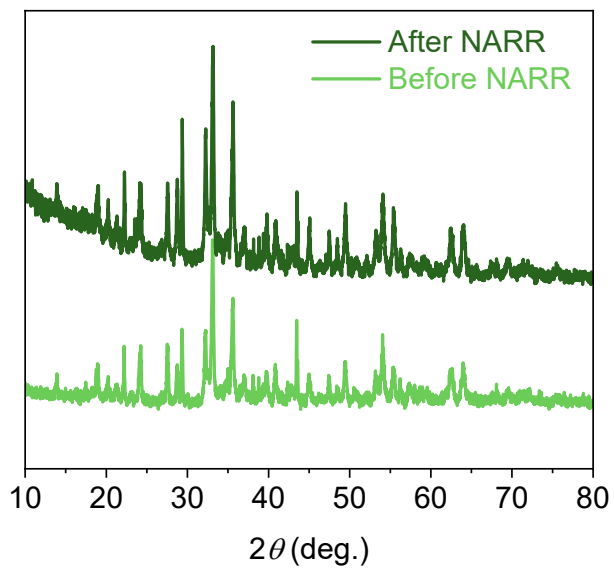
Fig. S10 XRD patterns before and after NARR.
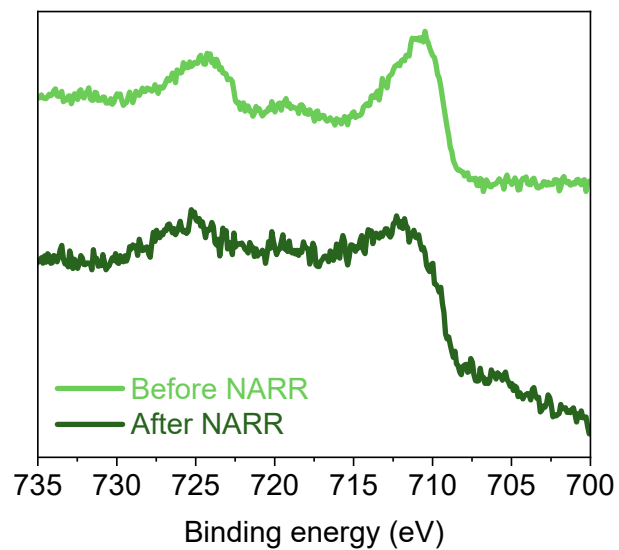

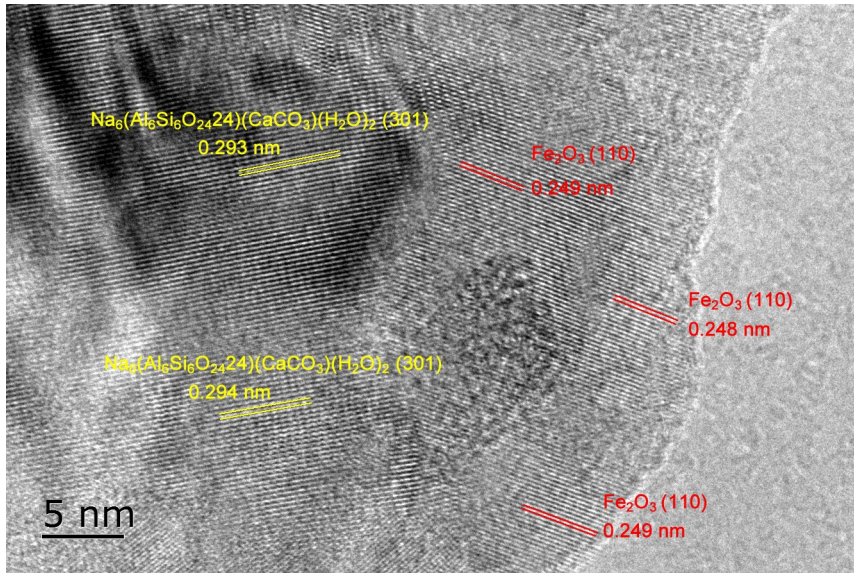**Fig. S11** Fe2p XPS profiles before and after NARR.

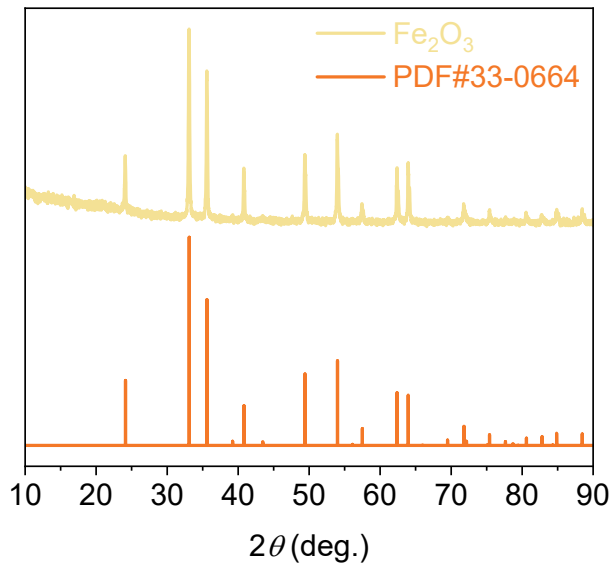**Fig. S12** HRTEM image of the RM sample after NARR test.

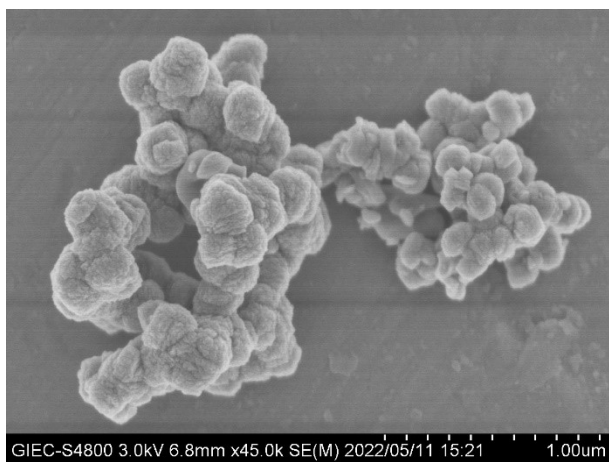**Fig. S13** XRD pattern for pure Fe_2O_3 sample.

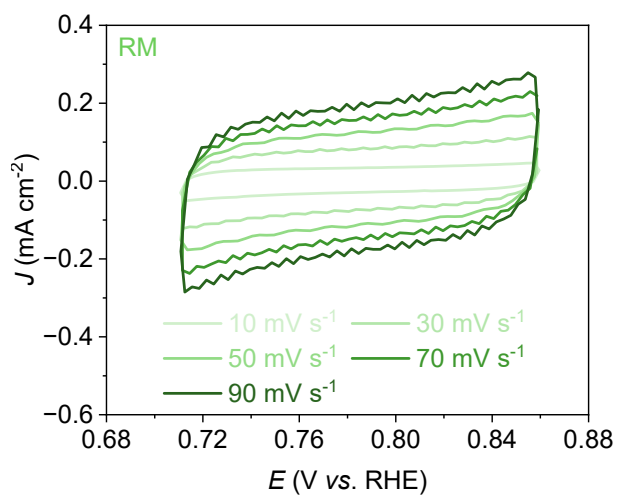**Fig. S14** SEM image for pure Fe$_2$O$_3$ sample.

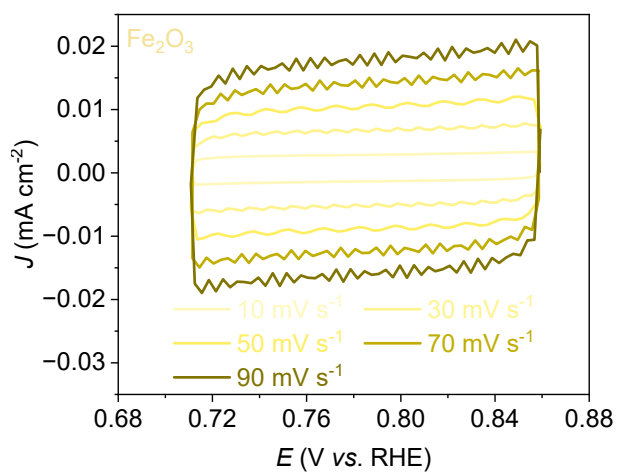**Fig. S15** CV test in non-faradaic range with different scan rates for RM.

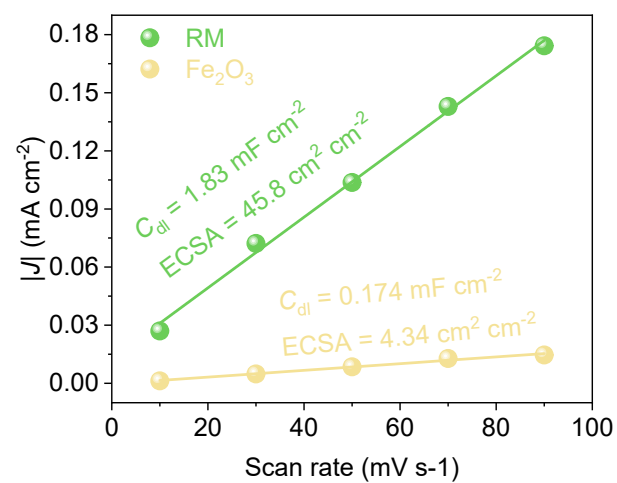**Fig. S16** CV test in non-faradaic range with different scan rates for pure Fe$_2$O$_3$ sample.

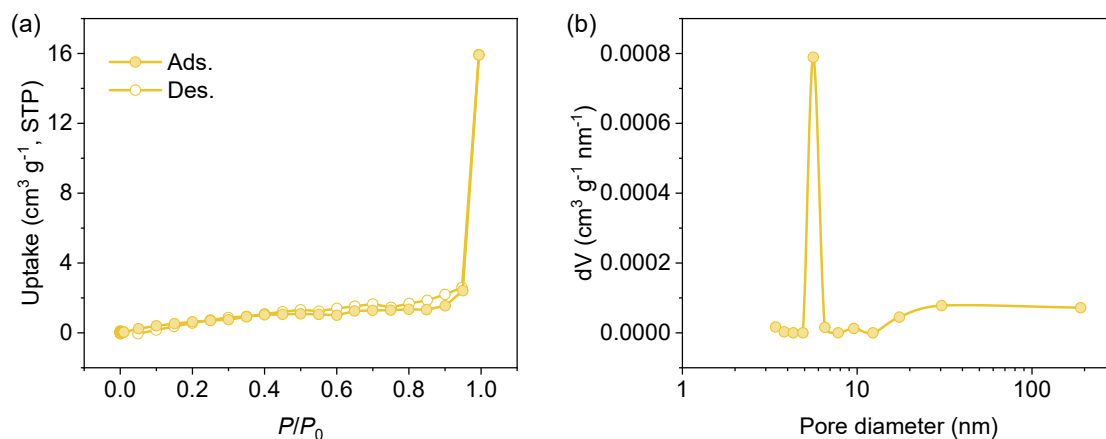**Fig. S17** ECSA fittings of RM and pure Fe$_2$O$_3$.

Fig. S18 (a) 77 K N_2 sorption isotherms of Fe_2O_3 and (b) the corresponding pore diameter distribution. From the isotherms it can be clearly observed that the surface area of Fe_2O_3 is smaller than RM, and the pore diameter distribution reveals only a small amount of mesopores with ca. 5.6 nm, consisting well with the ECSA results (Fig. S17).
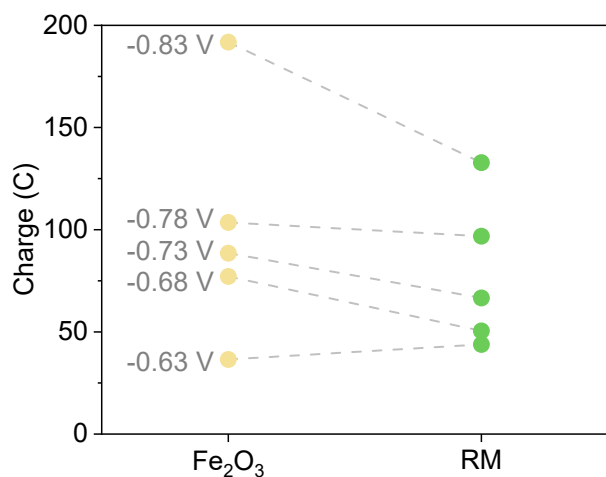

Fig. S19 Comparison of charge at different potentials between RM and pure Fe_2O_3.
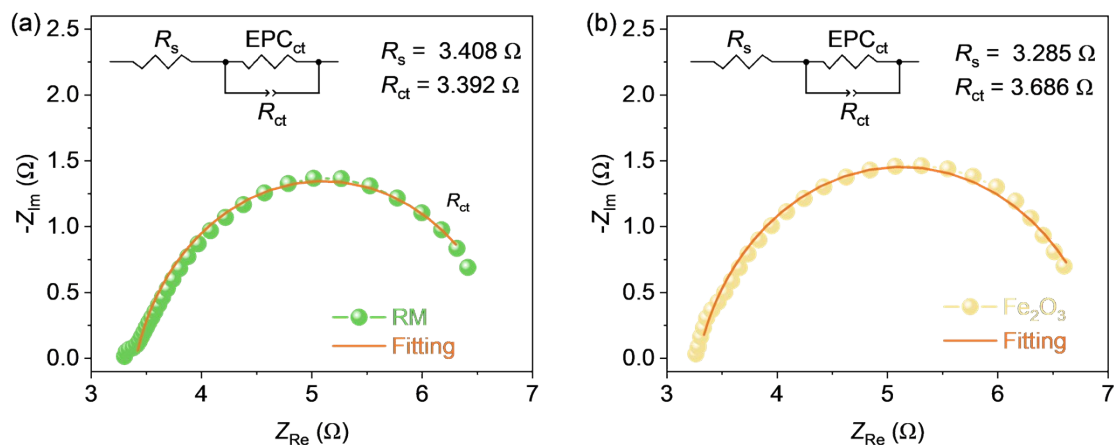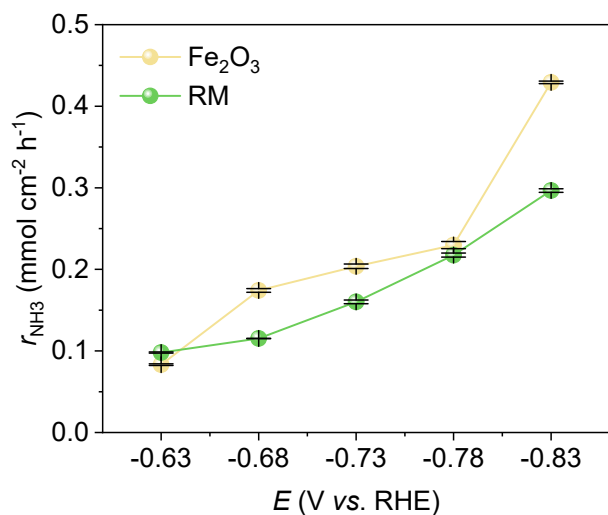
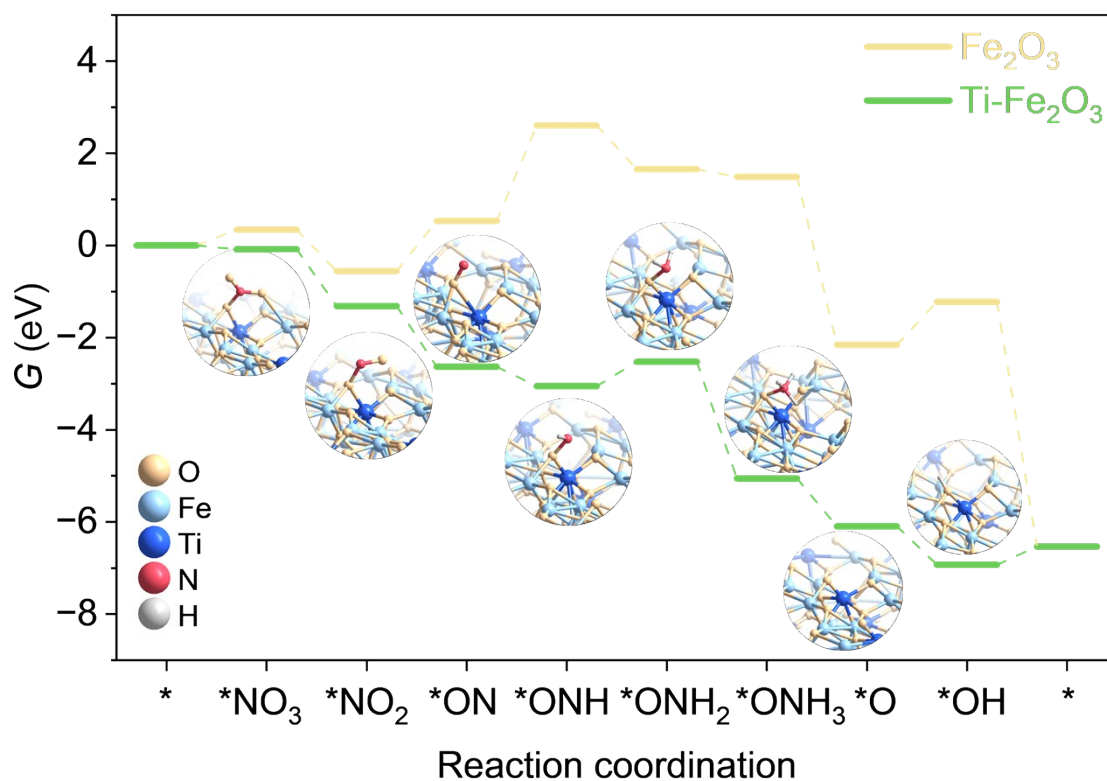**Fig. S21** Comparison of r_{NH3} at different potentials between RM and pure Fe$_2$O$_3$.

Fig. S22 Gibbs free energy diagram based on the DFT calculation for Fe$_2$O$_3$ and Ti-doped Fe$_2$O$_3$. Reaction pathway: * →

$*NO_3 \rightarrow *NO_2 \rightarrow *ON \rightarrow *ONH \rightarrow *ONH_2 \rightarrow *ONH_3 \rightarrow *O \rightarrow *OH \rightarrow *$. It can be found that the last step, the step of "*ON + H$^+$ + e$^-$ → *ONH", undergoes the highest Gibbs free energy (ΔG) change of +2.076 eV for Fe$_2$O$_3$. While the highest ΔG step is merely +0.529 eV for the Ti-doped Fe$_2$O$_3$. Therefore, results reveal that the dopant Ti atoms can insightfully drop the reaction barrier and thus enhance the NARR performance toward the increase of the NH$_3$ selectivity.

The overall electrocatalytic NARR process "NO$_3^-$ + 9H$^+$ + 8e$^-$ → NH$_3$ +3H$_2$O" can be described as nine elementary steps:

Step 1: * + NO$_3^-$ → *NO$_3$ + e$^-$	Step 2: *NO$_3$ + 2H$^+$ + 2e$^-$ → *NO$_2$ + H$_2$O
Step 3: *NO$_2$ + 2H$^+$ + 2e$^-$ → *ON + H$_2$O	Step 4: *ON + H$^+$ + e$^-$ →*ONH
Step 5: *ONH + H$^+$ + e$^-$ → *ONH$_2$	Step 6: *ONH$_2$ + H$^+$ + e$^-$ → *ONH$_3$
Step 7: *ONH$_3$ → *O + NH$_3$	Step 8: *O + H$^+$ + e$^-$ → *OH
Step 9: *OH → * + H$_2$O	

To avoid calculating the energy of charged NO$_3^-$ directly, gaseous HNO$_3$ is chosen as a reference (*Adv. Funct. Mater.* **2021**, *31*, 2008533; *ACS Catal.* **2022**, *12*, 8698–8706). As a result, the NO$_3^-$ adsorption can be described as * + HNO$_3$(g) → *NO$_3$ + H$^+$ +e$^-$.

Correspondingly, the adsorption energy of NO$_3^-$, which is defined as ΔG(*NO$_3$), can be approximated by ΔG(*NO$_3$) = G(*NO$_3$) − G(*) -G(HNO$_3$, g) + 1/2 G(H$_2$) + 0.3917 eV

where G(*NO$_3$) is the Gibbs free energy of NO$_3^-$ adsorbed on catalysts; G(*) is the free energy of catalysts, and G(HNO$_3$, g); G(H$_2$, g) are the free energy of HNO$_3$ and H$_2$ molecules in the gas phase, respectively.

In the view of computational hydrogen electrode (CHE) model, the ΔG of each elementary step is defined as ΔG = ΔE + ΔZPE −$T\Delta S$ + ΔG_{pH}

where ΔE denotes the energy change obtained from DFT calculations; ΔZPE and ΔS are the correction of zero-point energy and entropy, respectively; T is equal to 298.15 K. The pH effect can be corrected by ΔG_{pH} = pH × $k_B T$ln10.
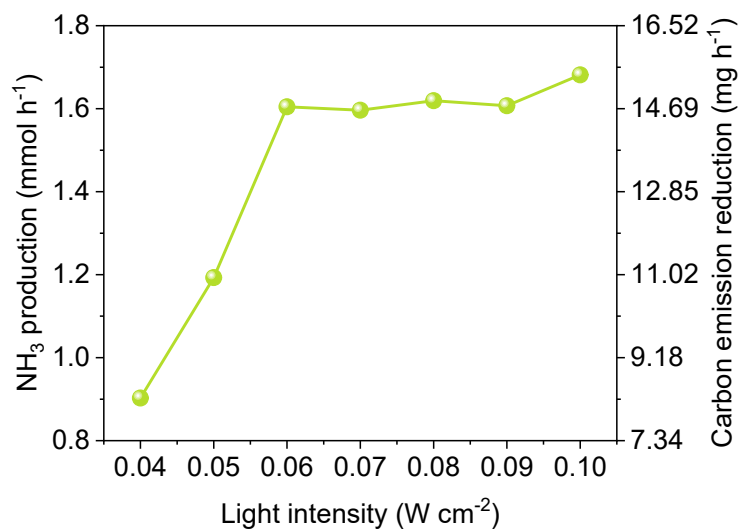
Fig. S23 Solar-driven NARR in NH_3 production as well as carbon emission reduction under different light intensities. Notably, the carbon emission reduction was calculated based on the carbon footprint (about 2.16 tons of CO_2 emission per ton of NH_3 produced) in Haber-Bosch process.[1, 2]

Table S1. Comparison of NARR performance between RM and other reported NARR catalysts.

Catalysts	Mediums	E / V vs. RHE	FE_{NH3} / %	r_{NH3} / mmol cm^{-2} h^{-1}	EE_{NH3} / %	Electric power consumption / kWh kg$_{NH3}^{-1}$	References
RM	1 M PBS + 1 M KNO$_3$	-0.73	92.8	0.16	33.2%	29.4	This work.
Fe$_3$O$_4$/SS	0.1 M NaOH + 0.1 M NaNO$_3$	-0.5	91.5	0.596	-	-	*Nano Res.* **2022**, *15*, 3050
Co-doped Fe/Fe$_2$O$_3$	0.1 M Na$_2$SO$_4$ + 500 ppm NO$_3^-$-N	-0.75	85.2	0.0886	-	-	*Proc. Natl. Acad. Sci. U.S.A.* **2022**, *119*, e2115504119
FeOOH/CP	0.1 M PBS + 0.1 M NaNO$_3$	-0.5	92	0.053	-	-	*ACS Appl. Mater. Interfaces* **2022**, *14*, 17312
2D Fe-cyano	1 M KOH + 0.1 M KNO$_3$	-0.5	90.2	4.95	26.2	-	*ACS Nano,* **2022**, *16*, 1072
TiO$_2$ microspheres	1.0 M PBS + 0.4 M KNO$_3$	-1.0	90.5	0.160	-	-	*ChemSusChem* **2022**, e202102450
Fe-doped Co$_3$O$_4$	0.1 M PBS + 50 mM KNO$_3$	-0.7	95.5	0.0367	-	-	*J. Colloid Interface Sci.* **2022**, *615*, 636
Fe-PPy SACs	0.1 M KOH + 0.1 M KNO$_3$	-0.7	98.4	0.16	27.5	24.38	*Energy Environ. Sci.* **2021**, *14*, 3522
Fe SAC	0.50 M KNO$_3$ + 0.10 M K$_2$SO$_4$	-0.66	75	0.308	-	-	*Nat. Commun.* **2021**, *12*, 2870
Strained Ru nanoclusters	1 M KOH + 1 M KNO$_3$	-0.2	~100	1.029	26.6	25.6	*J. Am. Chem. Soc.* **2020**, *142*, 5702
Cu-Ni alloy	1 M KOH + 1 M KNO$_3$	-0.15	~100	4.16	29.71	17.41	*J. Am. Chem. Soc.* **2020**, *142*, 5702
Cu/Cu$_2$O	0.5 M	-0.85	81.2	0.24	16.01	26.23	*Angew. Chem.*

nanowire arrays	Na$_2$SO$_4$ + 200 ppm NaNO$_3$-N						*Int. Ed.* **2020**, *59*, 5350
O-Cu–PTCDA	0.1 M PBS + 500 ppm KNO$_3$	-0.4	77	0.0256	19.37	20.56	*Nat. Energy* **2020**, *5*, 605
Au/C	0.5 M K$_2$SO$_4$ + 1 mM KNO$_3$	-0.3	26	1.58 × 10^{-3}	6.97	19.30	*ACS Energy Lett.* **2020**, *5*, 2095
TiO$_{2-x}$ NTs	0.5 M Na$_2$SO$_4$ + 50 ppm nitrate N (NaNO$_3$)	-1.6 (*vs.* SCE)	87.1	0.045	16.43	27.41	*ACS Catal.* **2020**, *10*, 3533

References

1. C. Kurien and M. Mittal, *Energy Convers. Manag.*, 2022, **251**, 114990.
2. S. Ghavam, M. Vahdati, I. A. G. Wilson and P. Styring, *Front. Energy Res.*, 2021, **9**, 580808.